Benefits of high-density electromyography for spinal moment estimation via musculoskeletal modeling

Ali Ghasem Zadeh Khoei[1], Alejandro Moya-Esteban[1], Bert-Jan Van Beijnum[2], Massimo Sartori[1]

***Abstract*— Bipolar electrodes that record the electrical signals of the muscles have been the most common approach of surface muscle activity measurement in the past. In recent years, high-density electromyography (HD-EMG) has shown to have its advantages in recording EMG signals of the muscles with considerably large areas. Previous EMG-driven models have been used to analyze lumbosacral joint moments; however, none of them was driven by HD-EMG, and therefore, it is unclear to what extent HD-EMG technology can benefit the analysis of joint moments. In the current study, we assessed effect of bipolar EMG (BP-EMG), HD-EMG and a new method of processing HD-EMG based on watershed algorithm for each muscle in driving a large-scale HD-EMG-driven model of trunk muscles to estimate the L5-S1 joint moments during different symmetric lifting tasks. We also compared the differences at EMG levels of BP-EMG and HD-EMG. Moreover, we provided a highly accurate map of thoracolumbar muscle activity during these movements using 512 HD-EMG channels (256 electrodes on each side of the spine). During our experiment, subject's kinematics, ground reaction forces, HD-EMGs of thoracolumbar muscles and BP-EMGs of abdominal muscles were used in estimation of L5-S1 joint moment through inverse dynamics and HD-EMG driven modelling. One healthy male subject performed symmetric box lifting tasks with 5 and 15 kg weight using squat and stoop techniques. We found 0,88 average correlation coefficient (R^2) between the reference moments from ID and estimated joint moments using HD-EMG recordings and the root mean squared errors (RMSE) ranging from 19.23 to 25.07 Nm. This study represents the first step for developing a framework that allows estimating thoracolumbar joint moments which has the potential to be used together with emerging embedded textile electrodes, eliminating the need for palpation of spine to locate the precise sites of bipolar electrode placements.**

***Index Terms*— Exoskeleton, EMG-driven Modeling, high-density electromyography**

I. INTRODUCTION

Low back pain (LBP) is a prevalent and disabling work-related musculoskeletal complaint encountered in variety of industries. The point prevalence of low back pain (LBP) in 2017 was estimated to be about 7.5% of the global population, or around 577.0 million people [1]. It is also estimated that between 70% and 85% of the population suffer from at least one low back pain episode in their live [2]. Epidemiological studies reveal that LBP is related to awkward postures, including trunk flexion with or without rotation, combined trunk flexion and manual lifting, frequent trunk bending and prolonged static trunk flexion [3]. This will not only affect the quality of life of the workers but also burdens economical detriments to care-taking institutes and employers through diagnosis, treatment, or in the worst case by replacing employees.

Due to the advances in technology fields such as mechanical engineering, biomedical engineering, electronic engineering and artificial intelligence, robotic exoskeleton technology has acquired rapid development in recent years [4]. Exoskeletons developed significantly to be used for human power augmentation and robotic rehabilitation by means of producing assistive forces and torques to the human joints [4]. In the clinical setting, exoskeletons can be used in the rehabilitation of post-stroke patients and patients with sensory-motor impairments to recover their lost abilities [5]. Besides clinical use, there is also a military use of exoskeletons in dismounted combatants who need to carry weights with high proportion to their weight [6]. As a result of successful medical and military developments of exoskeletons, there has been a huge upsurge in the industrial use of robotic exoskeletons in recent years [7]. Industrial robotic exoskeletons aim to reduce the mechanical loads that the workers endure during physically demanding tasks and, therefore, reduce the incidence of musculoskeletal injuries and resulting financial burden [7]. Back-support exoskeletons were developed in order to assist back muscles and support them in a way that reduces the risk of musculoskeletal injuries and especially LBP. Previous studies have shown that back-support exoskeletons can reduce the amount of physical load on the back muscles about 10% to 40% by lowering the muscular activities [8]. The amount of decrease in physical load depends on the ability of the exoskeleton to provide assistive torque while retaining the moveability of the wearer. Since active devices have more potential in providing assistive forces and torques in a controlled manner, they might have better performance in reducing the physical load of muscles and the spine.

1 Department of Biomechanical Engineering, University of Twente, Enschede, The Netherlands
2 Department of Electrical Engineering, Mathematics and Computer Science, University of Twente, Enschede, The Netherlands

Currently, there have been some studies that used different control strategies to control an active exoskeleton related to different parts of the body based on segment angles, interaction forces, muscle forces and a combination of these variables [9-14]. Being an open topic, there is no definite control strategy of a back-support exoskeleton for reducing the risk of LBP. However, some control strategies such as minimizing electromyographic (EMG) activity of back muscles have a physiological variable that can be measured using non-invasive techniques [12]. Since there is a highly non-linear relation between EMG and joint loading, a reduction in back muscle EMG does not necessarily result in a reduction in spinal loading [15]. On the other hand, it has been proven that the magnitude of back muscle forces directly affects the magnitude of the loading of intervertebral joints [12]. Hara et. al. studied the effect of muscle force on the lumbosacral (L5-S1) joint through a variety of lifting tasks [12]. Their study shows that the peak compression force on the aforementioned joint during lifting of 15kg box can go up to 6000N. However, to the best of our knowledge, there is no controller considering estimates of back muscle forces and spine compressive forces in their control action.

Another critical parameter in the back-support exoskeleton field that needs to be considered in the control strategy is the neuromechanics of the back muscles. Electrophysiological activation of a muscle leads to the production of mechanical force in that muscle [16]. This muscle activity can be measured by surface electrodes that show the EMG of muscles through electrical signals [16]. The classical method of recording such activity was using a bipolar (BP) electrode setup [17]. However, recording such muscles' activity by using BP electrodes can lead to misinterpreting results. This can be traced back to the nature of back muscles that have considerably wide areas and span over multiple joints. Therefore, collecting data from large muscles like those in the back with a bipolar electrode might not contain the full muscle activation patterns since these muscles do not activate heterogeneously [18,19]. In recent years, high-density electromyography (HD-EMG) has provided a new perspective on the field due to its potential to measure large areas. These potentials can be referred to as electrode size, inter-electrode distance, collection density, and collection surface [19]. While the first three parameters showed not to have a significant improvement in muscle force estimations, the collection surface showed remarkable improvement (25% decrease in root mean squared deviation between BP-EMG and HD-EMG) [19]. This would result in misinterpretation of muscle activation, which can be compensated using HD-EMG instead of conventional BP-EMGs.

To the best of our knowledge, no previous study has assessed the effects of driving an EMG-driven model representing the trunk with HD-EMG signals. In this paper, we will drive a large-scale EMG-driven model of the trunk by using a large-scale setup (512 HD-EMG channels) to estimate lumbar joint moments. Therefore, the goal of the present study is to provide, for the first time, a highly accurate map of thoracolumbar muscle activity during symmetric box lifting tasks by using a large set of HD-EMG signals. Then, we compared lumbosacral joint moments estimated using bipolar and high-density electromyography to validate our models. Based on the previously mentioned advantages of HD-EMGs, we hypothesize that by using the HD-EMG in estimating thoracolumbar joint moments, the joint moment estimation error will be reduced with respect to the gold standard, which is using bipolar to drive an EMG-driven model. However, since muscle activity is one primary input to the model, our secondary research question aimed at assessing fundamental differences at EMG levels of bipolar and high-density EMG configurations.

II. Methods

A. Subjects and Apparatus

The subject of this study was a 26 years old male participant with 68.0 kg weight, 175 cm height and without any background of low back pain. The experimental protocol was approved by the Ethics Committee of the University of Twente and the participant gave written informed consent.

To measure ground reaction forces (GRF) and moments, AMTI dual force-plate (AMTI, MA, USA) was used. During all experimental conditions, both feet of the subject were on the force plate (one leg on each side) and the sampling frequency of the recording was 2048 Hz.

Fig. 1. Subject of the experiment with four grids o electrode on each side of the spine. The reflective markers and EMG recording systems are attached and the subject is standing on the force plate.

The subject was being recorded through different box lifting tasks. Qualisys motion capture system (Qualisys Medical AB, Gothenburg, Sweden) was used to measure the kinematics of the full-body of the subject as well as the box. The 3D trajectories of 72 spherical reflective markers (64 on subject and 8 on each corner of the box) were recorded by 10 infrared Oqus cameras at a frequency of 128 Hz, see figure 1. Markers that were placed on the body of the subject can be divided into two groups: bony landmark markers and cluster markers (or so-called, triplets). The first group was used to scale a generic model to match participant's anthropometric characteristics and the second group was used to drive inverse kinematics. Thirty-seven markers that were used to scale the model were placed on: first and fifth metatarsal tuberosity, medial and lateral malleolus, calcaneus, medial and lateral femur epicondyle, anterior and posterior superior iliac spine, T10, T6 and C7 spinous process, sternum, clavicle, acromion, medial and lateral humerus epicondyle, ulna-styloid and radius-styloid process and second and fifth knuckles of the hand of both right and left side of the body. The remainder of markers were placed in a triangular order to track the subject's kinematics during inverse kinematics and were located on arm, forearm, thigh and shank. To track the hand, trunk, and foot; radius-styloid process and second and fifth knuckles of the hand; C7, acromion and clavicle, anterior and posterior superior iliac spine; and first and fifth metatarsal tuberosity and calcaneus markers were used, respectively.

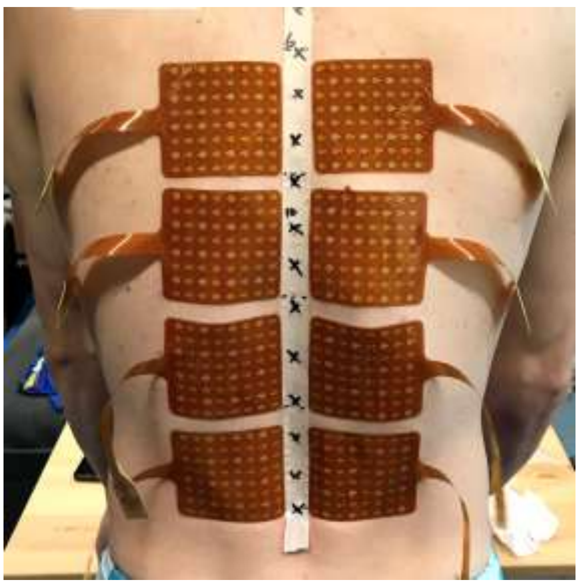

Fig. 2. Palpation of spinal processes and the adhered location of high-density electrodes.

During the experimental session (see part II-C), HD-EMG of erector spinae muscles and BP-EMG of abdominal muscles were measured, respectively. EMGs were measured using four Refa systems (TMSi, Oldenzaal, The Netherlands) and eight semi-disposable grids, each consisting of 64 electrodes placed in an 8×8 arrangement. These four Refas accounted for 536 channels consisting of 512 HD-EMG channels and 6 BP-EMG channels. Each of the grids had a surface of 71×76 mm2, electrodes size of 1 mm with an 8.5 mm inter-electrode distance. The electrodes adhered to the skin on both sides of the spine with a 1cm lateral distance. The low edge of the bottom grid was leveled with the L5 spinous process and adhered above the posterior iliac spine, see figure 2. The other three grids of each side adhered to the skin on top of each other with a 3-5 mm distance between them. This resulted in the upper border of the most top grid to locate about the height of the inferior angle of the scapula. The activities of abdominal muscles were recorded at the following locations: approximately 15 cm lateral to umbilicus, above the inguinal ligament, and approximately 2 cm lateral to umbilicus for external oblique, internal oblique, and rectus abdominis, respectively.

BP-EMGs, HD-EMGs, GRF, and marker trajectories were recorded with Qualisys Track Manager (QTM) software. Four digital signals going from the motion capture system to each of the four Refa systems were used to synchronize the data.

B. EMG-driven musculoskeletal modeling

To be able to investigate the differences between the recording of muscle activity via BP-EMG and HD-EMG, a musculoskeletal model was developed. For this purpose, a previously developed toolbox called Calibrated EMG-Informed Neuromusculoskeletal (NMS) Modelling Toolbox (CEINMS) [20] was used. The model that is obtained by CEINMS, will be later able to estimate the net L5-S1 joint moment through different experimental conditions with the focus being only on thoracolumbar muscles. These muscles consist of longissimus thoracic, longissimus lumborum, and iliocostalis lumborum. However, the model needs to be calibrated first.

The calibration process involved an open-source application named OpenSim [21] in which several biomechanical properties such as joint moments, muscle-tendon unit (MTU) length, and moment arms could be calculated using inverse kinematics (IK), inverse dynamics (ID), and muscle analysis (MA) toolboxes. These results, together with the EMG recordings, make the base for calibrating the CEINMS model. The base model that is used in OpenSim is also a previously validated musculoskeletal model [22]. This model is also known as the lifting full-body model (LFB) which consists of 30 different body segments with 29 degrees of freedom (DOFs) and 238 Hill-type MTUs that depute trunk muscles.

C. Experimental protocol

On the first hand, the participant was asked to shave any hairs on the back. However, before the start of the experiment, the skin was shaved to remove any potential remainders of hairs. Furthermore, the area was rubbed with specific skin wipes to remove dead skin or oily skin, potentially increasing the impedance between the skin and the electrodes. Afterward, the subject's spine was palpated to mark all the relevant processes of the spine to determine the desired placement of the electrode. After that, the electrodes adhered to the skin, as discussed in Section II-A. Two maximum voluntary contractions (MVCs) were captured while the subject was pushing against a static hindrance to the best of his power, once for his back muscles and once for abdominal muscles. Recording MVCs would enable us to normalize the EMG recordings to be compared to others. Then the reflective markers were placed on the skin in the way described in Section II-A. The subject was then asked to stand on the force plates in a static posture. After the static trial, the subject was instructed about the desired tasks. The tasks consist of two symmetric box (22×40×30 cm) lifting tasks with two different weights of 5kg and 15kg. The first task is called squat (SQ) lifting, which is going down flexing the knees with keeping the back as straight as possible and without the calcaneus leaving the ground. The second task is called stoop (ST) lifting, where the subject has to bent-over to grab the box while the knees are as straight as possible. This would lead us to a total number of 16 lifting trials in which the subject had to go down to grab the box, lift the box to the upright position for two repetitions within 20 seconds. The subject was provided with 1 minute of rest between each trial to avoid the fatigue effect. Moreover, to reduce the bias, trials were randomized based on technique and weight.

D. Data analysis

The 3D marker trajectories, ground reaction forces (GRF) and HD-EMG recordings, were processed using a MATLAB toolbox called MOtoNMS [23]. GRFs and marker trajectories were low-pass filtered with a cut-off frequency of 6 Hz.

OpenSim software [21] was then used to scale the LFB model to comply with the participant's anthropometric characteristics. The bony landmark markers that have been mentioned in Section II-A from the static trial were used to scale the model. After that, the 3D marker trajectories and the scaled model were used to run the inverse kinematics to obtain the joint angles. Later on, joint angles were used to run the muscle analysis to obtain the muscle-tendon unit length and moment arms of the desired muscles. The box's weight was considered as vertical external forces that apply to both hands equally and simultaneously as the half of box's weight for each hand. The onset of hands' external force was when the box markers disengaged the ground about 1 cm. External forces of hands, GRFs, and joint angles from IK were then used to run the inverse dynamics to obtain the joint moments; see figure 3. Being the gold standard in calculation of inverse dynamics, the results of ID became our reference to evaluate the joint moment estimations from our EMG-driven musculoskeletal model [24].

E. HD-EMG processing

Following the data-processing, first, noisy or zero channels of HD-EMG recordings were interpolated based on the adjacent channels. Interpolation had three different conditions in which the faulty channels were recalculated based on their locations. If the channel was located in the corners, three adjacent channels were considered, and if the channel was located on edges or in the middle, five and eight adjacent channels were considered, respectively. Secondly, the raw EMG signals were mean subtracted and band-pass filtered to the 30-300 Hz. Then they were rectified, and in order to get a linear envelope, a low-pass filter with a cut-off frequency of 6 Hz was applied to them. Finally, each HD-EMG channel was normalized based on the maximum values obtained from the MVC recordings of each specific channel, and to further smoothen the envelopes to obtain HD-EMG heatmaps, the moving root mean square (RMS) of each channel was calculated with a 250-millisecond window length. The processing steps mentioned above were applied to both BP-EMGs and HD-EMGs. The difference arises in the next step, where we used HD-EMGs and BP-EMGs separately as an input to drive our musculoskeletal model.

In order to calibrate and then drive the CEINMS model, we required a mapping between EMG recordings and LFB muscle model. While the common approach uses the BP-EMG, a new method uses HD-EMG to calibrate the model. Therefore, we provided two calibrated models based on common approach and the HD-EMG recordings. In the first place, the calibration of the model was done based on BP-EMG. Therefore, six muscles (longissimus thoracic, longissimus lumborum, and iliocostalis lumborum for both sides) for the back and six muscles for the abdominal area (rectus abdominis, internal oblique, and external oblique for both sides) were used to drive the 238 MTUs of the model. The virtual locations of bipolar configuration selected out of our HD-EMGs recordings were based on the distance of the grid from the spine, empty braid in the margin of the grid, and inter-electrode distances. Therefore, the following points considered to locate the relevant channels' number amongst all eight grids: 4 cm lateral to T10, 3 cm lateral to L1, and 6 cm lateral to L2 for longissimus thoracic, longissimus lumborum, and iliocostalis lumborum, respectively [15] (see figure 4). The located neighbor monopolar channels' raw EMG signals were then subtracted from each other to produce the BP-EMG configuration. Calibration of the model was then done by taking the first repetition of four different trials into account (squat 5/15 kg and stoop 5/15 kg). BP-EMGs, joint moments,

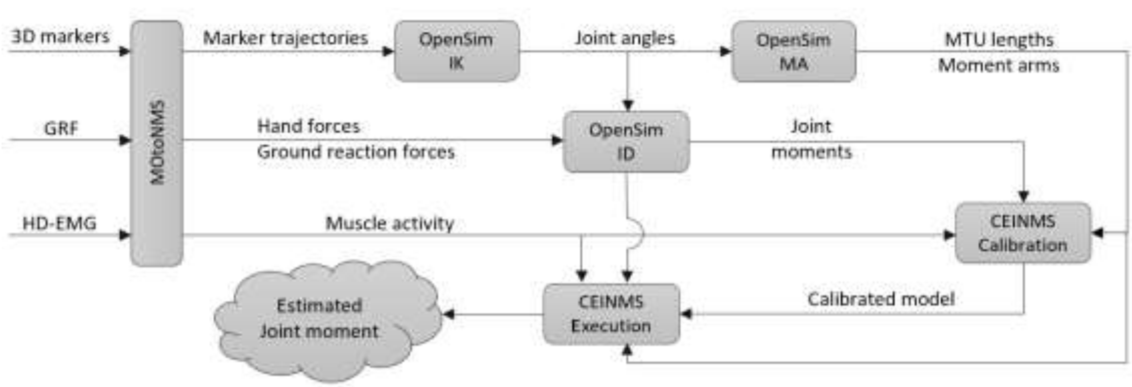

Fig. 3. General pipeline of the data analysis, consisting of MOtoNMS toolbox, OpenSim analysis, CEINMS calibration and CEINMS execution. The final outcome of the pipeline is the net estimated L5-S1 joint moment.

moment arms, and the MTU lengths of these four conditions were used to calibrate the model. The calibrated model was then driven based on BP-EMG, moment arms, MTU length and the inverse dynamic results to check on the ability of the model to estimate the net L5-S1 joint moment through 4×8 repetitions. In order to drive the CEINMS model based on HD-EMGs, we required a method to select and assign specific channels of our HD-EMGs to the muscles mentioned above to create a mapping between them.

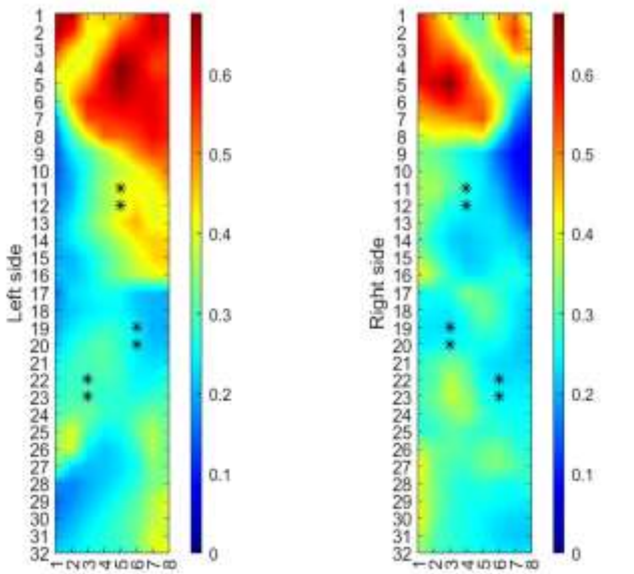

Fig. 4. Images depicting the high-resolution heatmaps of back muscles for squat with 15 kg at the time frame in which inverse dynamics L5-S1 joint moment peaked during box-lifting. The stars are locations of bipolar configuration in case of using bipolar electrodes for longissimus thoracic, longissimus lumborum and iliocostalis lumborum from top to bottom, respectively [15].

F. Watershed algorithm

The watershed technique in image processing had promising results in finding clusters of HD-EMG channels that compromise each other and represent one specific muscle's activity. Therefore, we decided to use "marker-controlled watershed segmentation" [25]. Watershed takes a gray-scale image and treats it as a surface where the lighter spots have high activations, and darker spots have low activations [26]. Then it locates the local maximums and, based on the diffusion of local activations, divides the surface into foreground and background and separates an image into specific segments [25,26]. Since the watershed uses a gray-scale image, the colored heatmaps were converted into gray-scale heatmaps, see figure 5, first row.

The next step was to decide which time frame to select as the reference point to apply the watershed onto it within the experiment's duration. Since we were going to use the clusters obtained at this step to drive the models, it has a substantial role. Thus, we produced heatmaps of three specific points based on the joint moments that we previously acquired with ID. These points include two box lifting and lowering peaks and the moment where the subject was standing while holding the box. Then based on the results of applied watersheds to them (see figure 5), we decided to select a specific time frame

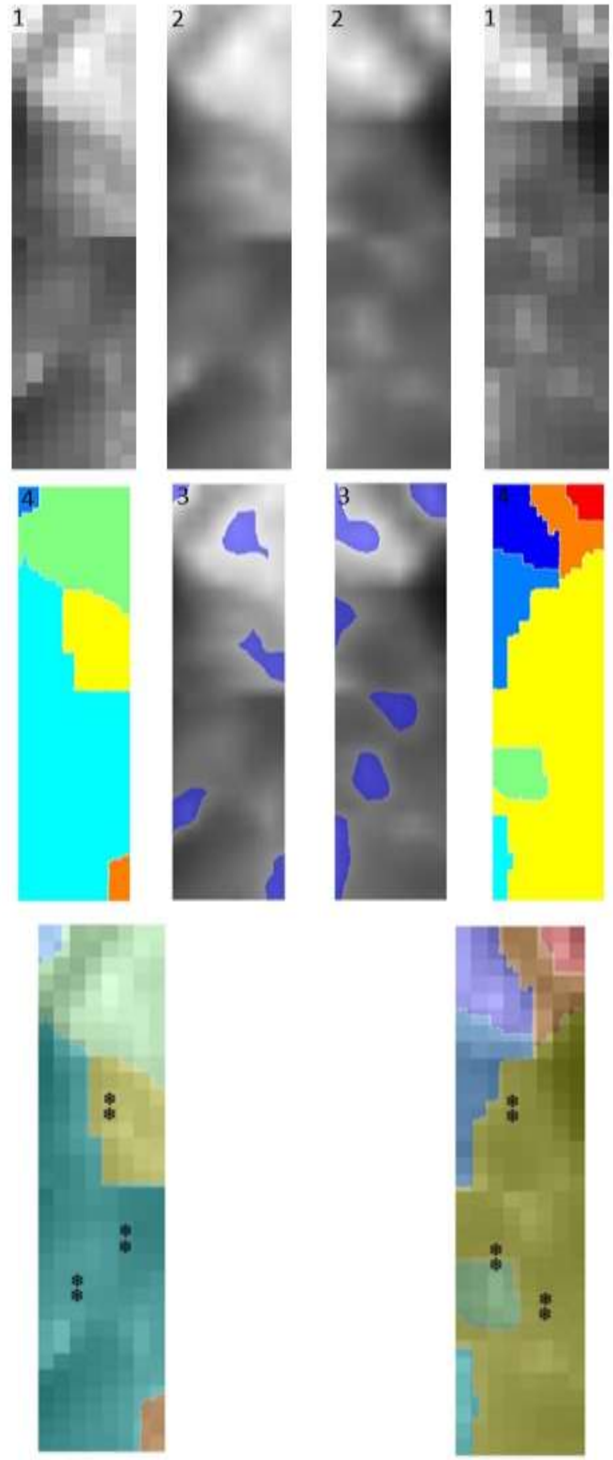

Fig. 5. These images depict the steps that the watershed algorithm takes to produce clusters of HD-EMG channels. Images marked in 1 are the original gray-scale heatmaps of back muscles. Images marked in 2 are the resolution increased heatmaps of back muscles. Third images show the local maximums and the adjacent pixels that have close activations to them. Fourth images depict the clusters that are made by algorithm based on detected maximum and local minimums. The two bottom images consist of two layers that overlap each other. The base layer is the gray-scale heatmap of the back muscles (can be seen in the middle images), and the overlapping layer is the result of the watershed algorithm that shows each segment with a specific color. The stars are locations of bipolar configuration in case of using bipolar electrodes for longissimus thoracic, longissimus lumborum and iliocostalis lumborum from top to bottom, respectively [15].

as a reference point. The process was applied to one repetition for each of the 4 experimental conditions (squat 5/15 kg and stoop 5/15 kg). This way, we obtained six clusters of channels for our six focused muscles for each of the experiment conditions, giving us cumulative 6×4 clusters. Since the clusters of channels within the heatmaps of all four conditions followed similar patterns, the highest peak of either lifting or lowering was selected as the reference time frame within the trial's duration. For each reference time frame, the watershed algorithm found a set of clusters of channels that later on we mapped to specific muscles, and the same cluster of channels was used to drive a muscle for the rest of trials (three remaining trials of each experimental condition). We obtained six specific clusters for each of our four conditions, different from the clusters of other conditions. HD-EMG channels within each cluster were averaged to obtain the final signal that will drive the EMG-driven musculoskeletal model; see figure 5. The way to map cluster of channels to muscles was by checking which cluster of markers laid on the position where a bipolar electrode would have been placed. Hereafter, these results will be referred as HD-EMG inputs of the CEINMS execution to estimate the net L5-S1 joint moments.

To take a further step toward automation of our mapping between HD-EMGs and the model's muscles, we decided to implement a new method. Since, for each of the six muscles of our model, we had four different clusters of channels (based on four different experimental conditions), we overlapped the clusters and only took those that were common to the four experimental conditions. We also overlapped previously mentioned clusters to obtain the union of each muscle's cluster channels, which consisted of all the present HD-EMG channels in either of the four clusters. We will call them high-density intersection (HDI) and high-density union (HDU) of EMG recordings, respectively. We had only six clusters that could be mapped to the model's muscles regardless of condition. Thus, we drove the model again, once using the HDI-EMGs of each muscle as an input to CEINMS execution and once using the HDU-EMGs of those muscles to estimate net L5-S1 join moments.

In the second place, the calibration of the model was done based on HD-EMGs. This would provide an excellent database to investigate the differences between joint moment estimations from BP-EMG calibrated model and HD-EMG calibrated model. Therefore, a selected group of channels based on the previously mentioned watershed method were assigned to desired muscles and, together with the joint moments, moment arms, and the MTU lengths of those muscles used as an input to calibration the model. Same as the first approach, the HD-EMG driven model was executed through BP-EMGs, HD-EMGs, HDI-EMGs, and HDU-EMGs of all trials.

In order to investigate our secondary research question, we compared the EMG recordings of BP, HD, HDI, and HDU EMG configurations, for each of six thoracolumbar muscles among all trials. Furthermore, to compare the results of model calibration based on BP-EMG and HD-EMG, we inquired the strength coefficients of the six relevant muscles between two calibrated models. strength coefficient is a parameter included in CEINMS that scales the maximum isometric force of the muscles in the EMG-driven model. This parameter is one of the parameters tuned in the calibration procedure.

The root mean squared error (RMSE) and R2 values were calculated between the reference L5-S1 joint moment that was achieved via OpenSim ID and the estimates of EMG-driven models via CEINMS. At the EMG level, EMG recordings of four configurations were divided based on configurations and conditions, and the average EMG amplitude was calculated for numerical comparison of muscle activity levels.

III. Results

A comparison of the net flexion-extension moment profiles of L5-S1 joint in BP-EMG, and HD-EMG calibrated CEINMS model that was driven with BP-EMGs, HD-EMGs, HDI-EMGs, and HDU-EMGs; with the OpenSim ID moments can be seen in figures 6 and 7. Comparison is made through symmetric box lifting cycle (LC). For the BP-EMG calibrated model, ID moments were approximately 10 Nm through all conditions at the beginning of the trials, suggesting that the subject was in a bit of flexion concerning the upright position. However, this pattern was different for the model's estimations. BP-EMG, HD-EMG, and HDI-EMG estimations started from approximately -2.75 Nm, -12.5 Nm, and -17 NM, respectively, which means that the subject was in small extension in the beginning. For the HDU-EMG estimations, there was a change between flexion and extension through different lifting techniques and weights. As it can be seen in the first row of figure 6, with the start of lifting the box, joint moment gradually raised to its maximum at about 25-30% of LC depending on the lifting condition and then reduced as the subject reached 50% of LC where he was standing in an upright position while holding the box for both ID and BP estimations. Moreover, with increased weight in the subject's hands, it can be seen in the plots that the calculated and estimated joint moments via ID and BP-EMG were higher when the subject was in an upright position (30 and 80 Nm for 5 and 15 kg). Results also show that the moment peaks for the stoop technique are slightly higher than that of the squat technique. Furthermore, while the BP-EMG followed ID to a reasonable extent in 5 kg conditions, for the 15 kg conditions, there is about 30 Nm shortcoming in maximum moment prediction for BP-EMG. The second row of figure 6 compares ID and HD-EMG estimations. Except for the stoop 15 kg condition, where there is almost no difference in L5-S1 joint estimation, the overall trend in this comparison is similar to the comparison between ID and BP-EMG. Lastly, it is clear that although the standard deviations for the 5kg conditions are pretty low for ID, BP-EMG and HD-EMG, in the case of 15 kg conditions, the standard deviation for BP-EMG and HD-EMG stands lower than ID.

The root mean squared error between ID reference moments and the rest of the configurations that were driven on the BP-EMG calibrated model can be seen in Table I. In the last column, the overall scores of each setup amongst all

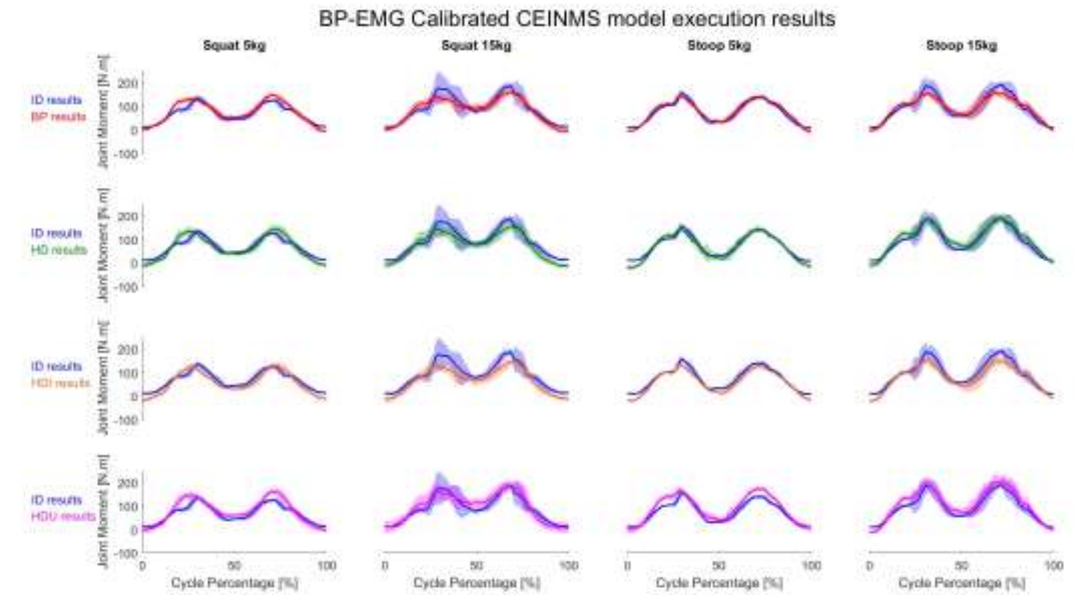

Fig. 6. Flexion-extension moments of the L5-S1 joint, calculated through inverse dynamics and estimated via CEINMS EMG-driven model. The model is calibrated with BP-EMG. Blue, red, green, orange and pink diagrams are the results of ID from OpenSim, CEINMS execution via BP-EMGs, HD-EMGs, HDI-EMGs, and HDU-EMGs respectively. Data are for four symmetric lifting conditions that discussed in section II-C. Solid lines show the mean of the moments of all repetition of each condition and shaded areas are ±1 standard deviation from the mean.

conditions are calculated. For all conditions, the lowest RMSE belongs to BP-EMG followed by HD-EMG (except for squat 5 kg where HDI-EMG has slightly lower RMSE). belongs to BP-EMG followed by HD-EMG (except for squat 5 kg where HDI-EMG has slightly lower RMSE). There is a fluctuation between HDI-EMG and HDU-EMG for having the highest RMSE among the four conditions. However, the lowest overall RMSE belongs to BP-EMG followed by HD-EMG, HDI-EMG, and HDU-EMG. Each setup's RMSE increased about 2 Nm concerning its previous one. It is also evident from the table that for the same weights, the stoop lifitng technique has always a lower RMSE than that of squat. R^2 values do not follow a clear trend between each setup or each condition. As it can be seen in the last column of Table I, overall R^2 values were the same for all four setups. This amount is 0.89 on average for the trials that were driven using BP-EMG calibrated model.

The estimated moment patterns for the model that have been

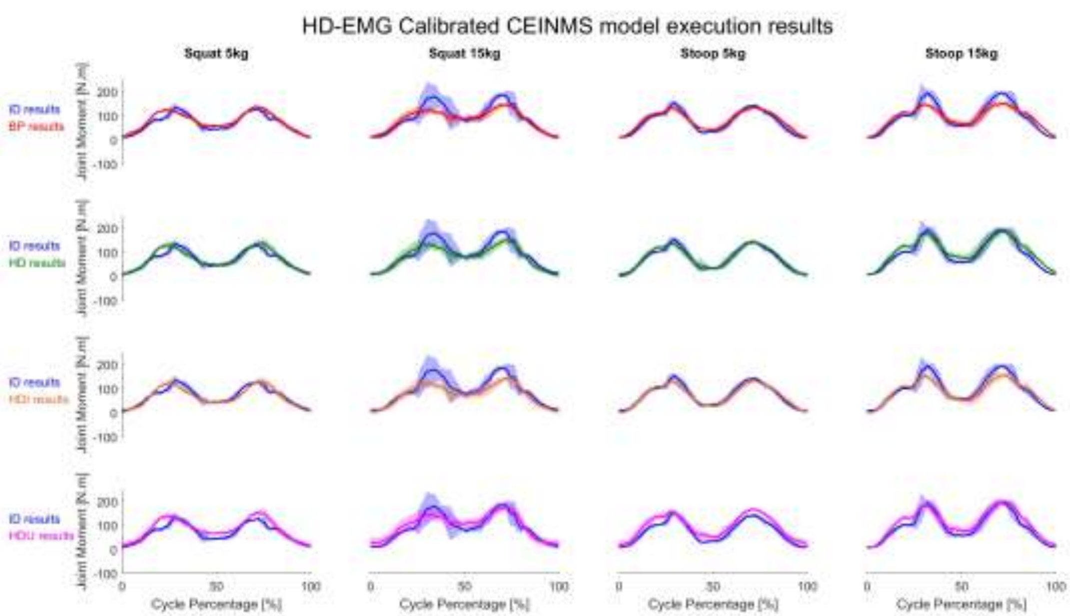

Fig. 7. Flexion-extension moments of the L5-S1 joint, calculated through inverse dynamics and estimated via CEINMS EMG-driven model. The model is calibrated with HD-EMG. Blue, red, green, orange and pink diagrams are the results of ID from OpenSim, CEINMS execution via BP-EMGs, HD-EMGs, HDI-EMGs, and HDU-EMGs respectively. Data are for four symmetric lifting conditions that discussed in section II-C. Solid lines show the mean of the moments of all repetition of each condition and shaded areas are ±1 standard deviation from the mean.

TABLE I
ROOT MEAN SQUARED ERROR (RMSE) AND R^2 BETWEEN ID AND BP-EMG, HD-EMG, HDI-EMG AND HDU-EMG JOINT MOMENT ESTIMATIONS OF BP-EMG CALIBRATED MODEL FOR ALL EXPERIMENTAL CONDITIONS

	RMSE				
	Squat 5kg	Squat 15kg	Stoop 5kg	Stoop 15 kg	Overall
Bipolar	17.41	26.89	11.83	20.79	19.23
High-Density	21.01	29.04	16.54	18.85	21.36
HD-Intersection*	20.00	32.47	16.56	24.35	23.35
HD-Unity*	24.75	28.62	23.79	23.14	25.07
	R-squared				
Bipolar	0.89	0.82	0.94	0.90	0.89
High-Density	0.86	0.84	0.92	0.93	0.89
HD-Intersection*	0.82	0.85	0.94	0.91	0.88
HD-Unity*	0.86	0.83	0.93	0.92	0.89

* This is the intersection/unity of the channels of each specific muscle among all conditions

calibrated using HD-EMG signals were similar to those in the estimations of our model that was calibrated with BP-EMG signals. A similar comparison between the ID results and different EMG setups of the HD-EMG calibrated model in estimating net L5-S1 joint moment can be seen in Table II and figure 7. In comparison between BP-EMG and HD-EMG, except for squat 5 kg, the HD-EMG has lower RMSE across the conditions. However, there is an alteration between HD-EMG and HDI-EMG in having the lower RMSE. In the case of HDU-EMG, RMSEs do not seem to follow a clear pattern. In an overall RMSE evaluation between setups, it is clear that the lowest RMSE belongs to HD-EMG, which is followed by HDI-EMG, and then comes the BP-EMG. HDU-EMG has the highest RMSE concerning other setups. In R2 value matching between four setups, there is not a recognizable gap between the setups, and their overall values are of the same order. An average amount of R2 for the trials that were driven using HD-EMG calibrated model, was standing at 0.88.

TABLE II
ROOT MEAN SQUARED ERROR (RMSE) AND R^2 BETWEEN ID AND BP-EMG, HD-EMG, HDI-EMG AND HDU-EMG JOINT MOMENT ESTIMATIONS OF HD-EMG CALIBRATED MODEL FOR ALL EXPERIMENTAL CONDITIONS

	RMSE				
	Squat 5kg	Squat 15kg	Stoop 5kg	Stoop 15 kg	Overall
Bipolar	15.59	31.22	13.07	24.39	21.06
High-Density	17.09	29.81	12.36	19.17	19.61
HD-Intersection*	15.74	32.65	11.64	23.21	20.81
HD-Unity*	22.27	28.24	23.93	21.58	24.00
	R-squared				
Bipolar	0.86	0.79	0.94	0.90	0.87
High-Density	0.84	0.82	0.93	0.93	0.88
HD-Intersection*	0.85	0.82	0.94	0.90	0.88
HD-Unity*	0.84	0.81	0.93	0.92	0.88

* This is the intersection/unity of the channels of each specific muscle among all conditions

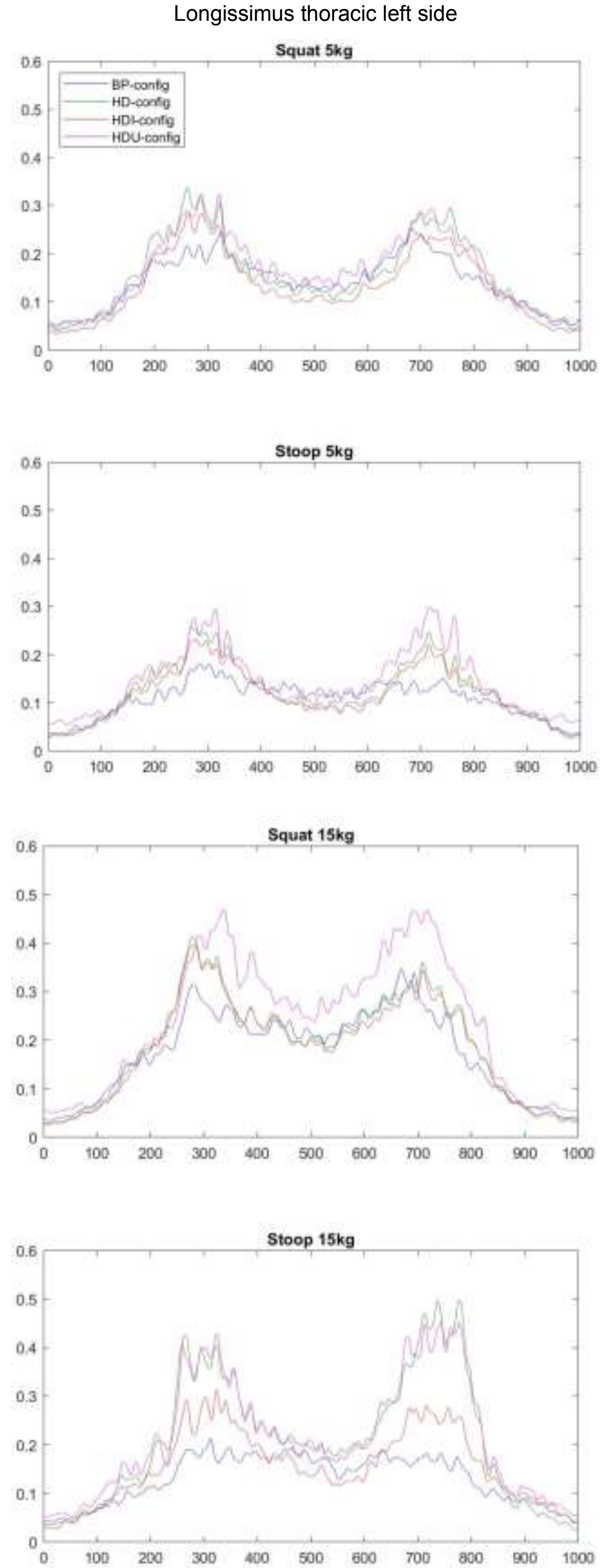

Fig. 8. Normalized EMG recordings of left longissimus thoracic muscle among four experimental conditions, and for BP-EMG, HD-EMG, HDI-EMG, and HDU-EMG configurations.

Results of the normalized EMG recordings of left longissimus thoracic among four experimental conditions and for BP-EMG, HD-EMG, HDI-EMG, and HDU-EMG are shown in figure 8. As shown in figure 8, for all experimental conditions, BP-EMG has the lowest overall activity, followed by HDI-EMG, HD-EMG, and HDU-EMG. Moreover, as was expected, the overall activity is higher in the case of the higher weights; however, there is no significant difference between squat and stoop techniques for 5 and 15 kg weights. Detailed plots of all six muscles can be found in the appendices. The average normalized EMG amplitudes of different configurations can be seen in Table III. For longissimus thoracic (right and left), HDU-EMG shows the highest activity, followed by HD-EMG, HDI-EMG, and BP-EMG. However, the trend changes for longissimus lumborum (right and left), with BP-EMG having the highest activity. Then comes the HDU-EMG, HD-EMG, and HDI-EMG, respectively. Considering the iliocostalis lumborum, although HDU-EMG has a higher amplitude than BP-EMG on the left side, the order is the same as longissimus for the rest of the configuration lumborum. The BP-EMG and HD-EMG, HDI-EMG, and HDU-EMG average amplitudes are within 19%, 25%, and 21% of each other, respectively.

Moreover, the comparison between strength coefficients of MTUs of the calibrated models with BP-EMG and HD-EMG relevant to our six focused muscles did not show any significant difference. The table of detailed strength coefficient values of both calibrated models can be fined in the appendices.

TABLE III
AVERAGE NORMALIZED EMG AMPLITUDES OF THE BP, HD, HDI, AND HDU CONFIGURATIONS AMONG DIFFERENT CONDITIONS

	Longissimus Thoracic left				Longissimus Thoracic right			
	BP	HD	HDI	HDU	BP	HD	HDI	HDU
SQ5	0.141	0.160	0.135	0.163	0.095	0.111	0.121	0.209
SQ15	0.177	0.191	0.185	0.242	0.121	0.184	0.169	0.303
ST5	0.108	0.124	0.116	0.144	0.081	0.118	0.106	0.236
ST15	0.130	0.211	0.155	0.218	0.096	0.219	0.137	0.232
Avg	0.139	0.171	0.148	0.192	0.098	0.158	0.133	0.245
	Longissimus Lumborum left				Longissimus Lumborum right			
	BP	HD	HDI	HDU	BP	HD	HDI	HDU
SQ5	0.201	0.160	0.126	0.154	0.160	0.111	0.102	0.136
SQ15	0.220	0.147	0.160	0.201	0.205	0.184	0.126	0.198
ST5	0.147	0.090	0.099	0.133	0.135	0.118	0.078	0.124
ST15	0.173	0.174	0.121	0.172	0.165	0.146	0.098	0.165
Avg	0.185	0.143	0.126	0.165	0.166	0.140	0.101	0.156
	Iliocostalis Lumborum left				Iliocostalis Lumborum right			
	BP	HD	HDI	HDU	BP	HD	HDI	HDU
SQ5	0.143	0.160	0.126	0.154	0.167	0.111	0.102	0.136
SQ15	0.179	0.147	0.160	0.201	0.214	0.184	0.126	0.198
ST5	0.126	0.090	0.099	0.133	0.139	0.118	0.078	0.124
ST15	0.156	0.174	0.121	0.172	0.190	0.146	0.098	0.165
Avg	0.151	0.143	0.126	0.165	0.177	0.140	0.101	0.156

IV. DISCUSSION

The primary goal of the current study was validating back musculoskeletal models to estimate lumbosacral joint moments based on HD-EMG and compare the results with BP-EMG. Based on the previously validated pipeline [15], we used the CEINMS toolbox together with HD-EMG and BP-EMG to separately calibrate two musculoskeletal models. We used one trial of each condition (squat 5/15 kg and stoop 5/15 kg) to calibrate our model, once using BP-EMG as input and once using HD-EMG. Then we used each of calibrated models to estimate the net L5-S1 joint moment using BP-EMG, HD-EMG, HDI-EMG, and HDU-EMG as input for different symmetric box lifting tasks. This means that once we calibrate the model based on a set of existing movements in the beginning, we can use the model to estimate the lumbosacral joint moments later on regardless of the motion condition. The reason for considering using HDI-EMG and HDU-EMG to estimate joint moments was that using these configurations we could assign a single cluster common for all conditions to a muscle through all conditions instead of assigning a specific cluster to each muscle for each of the conditions. Then we compared these results to the ID gold standard.

Our results show a high correlation and low RMSE between ID and CEINMS estimations. This confirms the compliance of our estimations with the ID. We had a lower RMSE for the stoop lifting technique than for squat can be traced back to the calibration process. Our calibration optimized the muscle force with more focus on highly flexed postures such as stoop rather than squat, resulting in better estimations for the stoop technique. Moreover, the results were not surprising since we expected the setup with which we calibrated the model to have the lowest RMSE. However, it is worth to be mentioned that the highest HDU-EMG RMSE in both calibrations suggests that taking a union of each muscle's relevant channels is somehow disrupting our applied watershed algorithm to classify each muscle's EMG. This is because taking a unity of each muscle's cluster within four experimental conditions gives a large cluster consisting of 94% and 77% of all EMG channels for thoracic and lumbar parts, respectively. Therefore, taking a union of each muscle's cluster could result in spoiling our clustering algorithm. Another critical point is that the magnitude of RMSE of BP-EMG and HD-EMG, in both calibration methods, stands at about 10% compared to the maximum moment. While the RMSE reveals the magnitude of the error between two trials, R2 concerns the joint moment profiles of the trials. High and close R2 values for both calibration conditions and different EMG setups prove that all estimations can mirror the ID joint moment profile to a reasonable extent. This is an essential point since a common exoskeleton's control strategy consists of producing torques on a specific joint based on its torque profile and a percentage of its maximum torque [4]. This means that our models have the potential to be implemented in the control strategy of an exoskeleton.

Based on joint moment profiles, at the beginning of the trials, when the subject is upright, there is a deviation of the joint moment from zero (slight flexion for ID and small extension for CEINMS estimations; see Section III). This could be due to some errors in ID and CEINMS computations. When the subject halts straight without carrying any weights, the muscle activity is at its lowest; therefore, the other parameters such as passive muscle force and muscle geometry are the main parameters that affect the joint moment. Anthropometry scaling of the LFB model used in ID calculations can be improved by using medical imaging techniques to increase the accuracy of the ID. The current

CEINMS calibrations were done based on only dynamic trials; therefore, it was not unexpected to have greater errors compared to inverse dynamic in estimations of the joint moment in static postures. The ID calculated and CEINMS estimated joint moment profiles also suggest that the HD-EMG has advantages in estimating maximum moments, especially in the stoop technique with higher weight. This means that using HD-EMG improved moment estimation for stooped postures. In this case, the maximum moment peak estimation error for BP-EMG and HD-EMG calibrated models are 33 and 44 Nm, respectively, while this magnitude is 2 and 9 Nm for the estimation of HD-EMGs. Moreover, these profiles depict about 10% increment in L5-S1 joint moment for squat and stoop technique, with stoop being higher. This increment seemed higher when we increased the weight from 5 kg to 15 kg for each squat and stoop technique by 50 Nm and 40 Nm, respectively. This means that our model is reacting to the changes in weights and conditions to a reasonable extent.

EMG level analysis of the recordings was performed to investigate how the difference in EMG activity could affect the joint moments. The results show that for the lumborum regions of iliocostalis and longissimus BP-EMG has higher activity than HD-EMG which should in return result in higher joint moment estimation using BP-EMG. However, our results show that this does not hold necessarily. The reason to this is the highly non-linear relation between muscle activity and joint moments. The passive force production of MTUs and simultaneous activation of agonist and antagonist muscles could result in production of same joint moments while the activity of the muscles are not the same. EMG recordings of thoracic part of longissimus show that the HD-EMG activity is higher than that of BP-EMG in this area. A possible explanation for this is that due to a large cluster that the watershed algorithm provided in thoracic region, and by averaging the EMG channels of this cluster, we also exerted the activity of lower trapezius muscle in our EMG input which was supposed to only belong to longissimus thoracic. Since the lower trapezius muscle is also involved in lifting tasks, having a large area of channels in this region results in higher activity than longissimus thoracic per se. This is in agreement with a previous study that applied pre-processing techniques such as gradient, smoothed gradient, and equalization to the base grey-scale heatmap of muscle activity, indicating that in some cases, the clustering could improve [27].

One main limitation of the current study is the limited sample size. This means that the subject was a young, healthy man, and therefore, the results cannot be interpreted for another age group or sex. The other limitation is the basic watershed algorithm, which has limited potential to cluster adjacent active regions precisely and provides a single region instead of two. This is evident in clustering failure in the thoracic region in our HD-EMG, where the activation of the lower trapezius was also considered.

It is evident from the results that there is no significant difference in driving our model using HD-EMG intersection/union or BP-EMG to estimate joint moments (only 2 Nm and 4 Nm difference in RMSE on average, respectively, and 1% difference in R2). This means that the HD-EMG reflects the behavior of the selected BP-EMG signals for lumbar musculature. However, despite the differences in activity levels for thoracic musculature, no significant moment differences in joint moment estimations were found. It can also be concluded that the present difference in joint moment estimations via BP-EMG and HD-EMG could track back to the differences in the activity of thoracic regions. Therefore, in our future research, we will further investigate the effect of thoracic and lumbar muscle forces in lumbosacral joint moments. Furthermore, we will use a priori information to match the obtained clusters via a watershed algorithm with the relevant muscles, which could result in the elimination of palpation requirement.

We could use the 6 clusters that were obtained via our method to map from HD-EMG to model's muscles of all conditions instead of specific clusters of each condition (24 clusters in total).

Some studies have shown promising results in controlling myoelectric prostheses by using embedded textile electrodes [28]. Therefore, we could use these emerging technologies in combination with our methodology to drive control strategies of a back-support exoskeleton in the future. Thus, by using an embedded textile electrode in a t-shirt, we only need to record the EMG activity of trunk muscles and run the watershed algorithm for different movements and locomotion. Then, once we compute the intersection/union of channels, we could estimate joint moments for all conditions, with only 3.5% error on average, by calibrating the model with HD-EMG without the need to have the BP-EMGs, which is the current gold standard.

V. Conclusion

Overall, we can conclude that using HD-EMG recording instead of common BP-EMG, and applying our developed methodology to the dataset to use 40-50% of the whole channels, does not reduce the accuracy of estimating lumbosacral join moments significantly. Moreover, although there is a difference in EMG activity level of the thoracic region due to limitations of the watershed algorithm, the final moment estimations did not change drastically. This implies the importance of the lumbar muscles in joint moment estimations. The current study also represents the first step in development of a framework that uses images processing techniques together with the EMG-driven musculoskeletal models, which has the potential to combine with embedded EMG textiles to estimate lumbosacral joint moments. This will, in return, allow control of exoskeletons without the need for precise palpation of the spine.

References

[1] Wu, Aimin, Lyn March, Xuanqi Zheng, Jinfeng Huang, Xiangyang Wang, Jie Zhao, Fiona M. Blyth, Emma Smith, Rachelle Buchbinder, and Damian Hoy. "Global low back pain prevalence and years lived with disability from 1990 to 2017:

estimates from the Global Burden of Disease Study 2017." *Annals of translational medicine* 8, no. 6 (2020).

[2] Biyani, Ashok, and Gunnar BJ Andersson. "Low back pain: pathophysiology and management." *JAAOS-Journal of the American Academy of Orthopaedic Surgeons* 12, no. 2 (2004): 106-115.

[3] Wong, Kelvin CH, Raymond YW Lee, and Simon S. Yeung. "The association between back pain and trunk posture of workers in a special school for the severe handicaps." *BMC musculoskeletal disorders* 10, no. 1 (2009): 1-8.

[4] Gopura, R. A. R. C., Kazuo Kiguchi, and D. S. V. Bandara. "A brief review on upper extremity robotic exoskeleton systems." In *2011 6th international Conference on Industrial and Information Systems*, pp. 346-351. IEEE, 2011.

[5] Bortole, Magdo, Anusha Venkatakrishnan, Fangshi Zhu, Juan C. Moreno, Gerard E. Francisco, Jose L. Pons, and Jose L. Contreras-Vidal. "The H2 robotic exoskeleton for gait rehabilitation after stroke: early findings from a clinical study." *Journal of neuroengineering and rehabilitation* 12, no. 1 (2015): 1-14.

[6] Mudie, Kurt L., Angela C. Boynton, Thomas Karakolis, Meghan P. O'Donovan, Gregory B. Kanagaki, Harrison P. Crowell, Rezaul K. Begg, Michael E. LaFiandra, and Daniel C. Billing. "Consensus paper on testing and evaluation of military exoskeletons for the dismounted combatant." *Journal of science and medicine in sport* 21, no. 11 (2018): 1154-1161.

[7] Bogue, Robert. "Exoskeletons–a review of industrial applications." *Industrial Robot: An International Journal* (2018).

[8] Toxiri, Stefano, Axel S. Koopman, Maria Lazzaroni, Jesús Ortiz, Valerie Power, Michiel P. De Looze, Leonard O'Sullivan, and Darwin G. Caldwell. "Rationale, implementation and evaluation of assistive strategies for an active back-support exoskeleton." *Frontiers in Robotics and AI* 5 (2018): 53.

[9] Fleischer, Christian, and Günter Hommel. "A human--exoskeleton interface utilizing electromyography." *IEEE Transactions on Robotics* 24, no. 4 (2008): 872-882.

[10] Giovacchini, Francesco, Federica Vannetti, Matteo Fantozzi, Marco Cempini, Mario Cortese, Andrea Parri, Tingfang Yan, Dirk Lefeber, and Nicola Vitiello. "A light-weight active orthosis for hip movement assistance." *Robotics and Autonomous Systems* 73 (2015): 123-134.

[11] Grazi, Lorenzo, Simona Crea, Andrea Parri, Raffaele Molino Lova, Silvestro Micera, and Nicola Vitiello. "Gastrocnemius myoelectric control of a robotic hip exoskeleton can reduce the user's lower-limb muscle activities at push off." *Frontiers in Neuroscience* 12 (2018): 71.

[12] Hara, Hiromasa, and Yoshiyuki Sankai. "Development of HAL for lumbar support." In *SCIS & ISIS SCIS & ISIS 2010*, pp. 416-421. Japan Society for Fuzzy Theory and Intelligent Informatics, 2010.

[13] Hayashi, Tomohiro, Hiroaki Kawamoto, and Yoshiyuki Sankai. "Control method of robot suit HAL working as operator's muscle using biological and dynamical information." In *2005 IEEE/RSJ International Conference on Intelligent Robots and Systems*, pp. 3063-3068. IEEE, 2005.

[14] Saccares, Lorenzo, Anais Brygo, Ioannis Sarakoglou, and Nikos G. Tsagarakis. "A novel human effort estimation method for knee assistive exoskeletons." In *2017 International Conference on Rehabilitation Robotics (ICORR)*, pp. 1266-1272. IEEE, 2017.

[15] Moya-Esteban, Alejandro, Niels P. Brouwer, Ali Tabasi, Herman Van Der Kooij, Idsart Kingma, and Massimo Sartori. "Muscle-level analysis of trunk mechanics via musculoskeletal modeling and high-density electromyograms." In *2020 8th IEEE RAS/EMBS International Conference for Biomedical Robotics and Biomechatronics (BioRob)*, pp. 1109-1114. IEEE, 2020.

[16] Disselhorst-Klug, Catherine, Thomas Schmitz-Rode, and Günter Rau. "Surface electromyography and muscle force: Limits in sEMG–force relationship and new approaches for applications." *Clinical biomechanics* 24, no. 3 (2009): 225-235.

[17] Lulic-Kuryllo, Tea, Francesco Negro, Ning Jiang, and Clark R. Dickerson. "Standard bipolar surface EMG estimations mischaracterize pectoralis major activity in commonly performed tasks." *Journal of Electromyography and Kinesiology* 56 (2021): 102509.

[18] Falla, Deborah, Leonardo Gizzi, Marika Tschapek, Joachim Erlenwein, and Frank Petzke. "Reduced task-induced variations in the distribution of activity across back muscle regions in individuals with low back pain." *PAIN®* 155, no. 5 (2014): 944-953.

[19] Staudenmann, Didier, Idsart Kingma, Dick F. Stegeman, and Jaap H. van Dieën. "Towards optimal multi-channel EMG electrode configurations in muscle force estimation: a high density EMG study." *Journal of Electromyography and Kinesiology* 15, no. 1 (2005): 1-11.

[20] Pizzolato, Claudio, David G. Lloyd, Massimo Sartori, Elena Ceseracciu, Thor F. Besier, Benjamin J. Fregly, and Monica Reggiani. "CEINMS: A toolbox to investigate the influence of different neural control solutions on the prediction of muscle excitation and joint moments during dynamic motor tasks." *Journal of biomechanics* 48, no. 14 (2015): 3929-3936.

[21] Delp, Scott L., Frank C. Anderson, Allison S. Arnold, Peter Loan, Ayman Habib, Chand T. John, Eran Guendelman, and Darryl G. Thelen. "OpenSim: open-source software to create and analyze dynamic simulations of movement." *IEEE transactions on biomedical engineering* 54, no. 11 (2007): 1940-1950.

[22] Beaucage-Gauvreau, Erica, William SP Robertson, Scott CE Brandon, Robert Fraser, Brian JC Freeman, Ryan B. Graham, Dominic Thewlis, and Claire F. Jones. "Validation of an OpenSim full-body model with detailed lumbar spine for estimating lower lumbar spine loads during symmetric and asymmetric lifting tasks." *Computer methods in biomechanics and biomedical engineering* 22, no. 5 (2019): 451-464.

[23] Mantoan, Alice, Claudio Pizzolato, Massimo Sartori, Zimi Sawacha, Claudio Cobelli, and Monica Reggiani. "MOtoNMS: A MATLAB toolbox to process motion data for neuromusculoskeletal modeling and simulation." *Source code for biology and medicine* 10, no. 1 (2015): 1-14.

[24] Matthew, Robert Peter, Sarah Seko, Ruzena Bajcsy, and Jeffrey Lotz. "Kinematic and kinetic validation of an improved depth camera motion assessment system using rigid bodies." *IEEE journal of biomedical and health informatics* 23, no. 4 (2018): 1784-1793.

[25] The MathWorks, Inc., 2022, *Marker-Controlled Watershed Segmentation*, accessed 14 February 2022, https://nl.mathworks.com/help/images/marker-controlled-watershed-segmentation.html

[26] Vieira, Taian MM, Roberto Merletti, and Luca Mesin. "Automatic segmentation of surface EMG images: Improving the estimation of neuromuscular activity." *Journal of biomechanics* 43, no. 11 (2010): 2149-2158.

[27] Vieira, Taian MM, Roberto Merletti, and Luca Mesin. "Automatic segmentation of surface EMG images: Improving the estimation of neuromuscular activity." *Journal of biomechanics* 43, no. 11 (2010): 2149-2158.

[28] Alizadeh-Meghrazi, Milad, Gurjant Sidhu, Saransh Jain, Michael Stone, Ladan Eskandarian, Amirali Toossi, and Milos

R. Popovic. "A Mass-Producible Washable Smart Garment with Embedded Textile EMG Electrodes for Control of Myoelectric Prostheses: A Pilot Study." *Sensors* 22, no. 2 (2022): 666.

APPENDIX

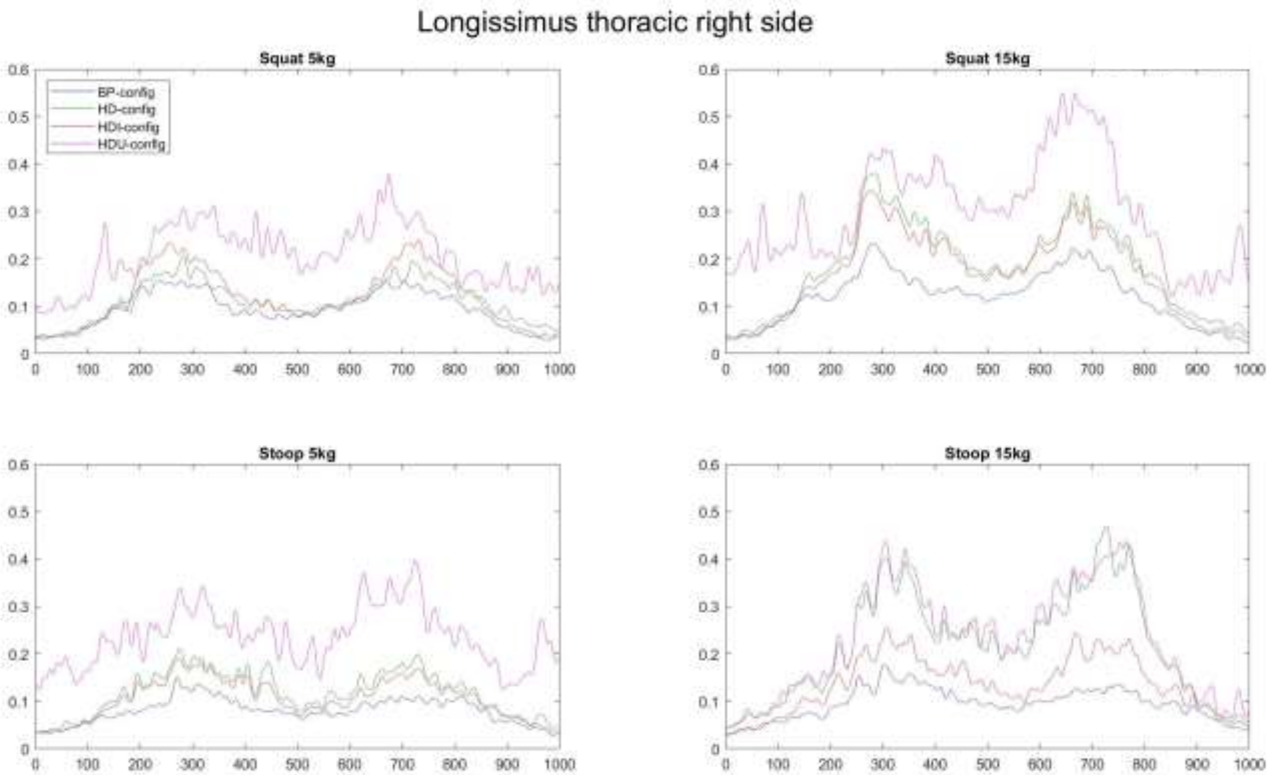

Fig. 1. Normalized EMG recordings of right longissimus thoracic muscle among four experimental conditions, and for BP-EMG, HD-EMG, HDI-EMG, and HDU-EMG configurations.

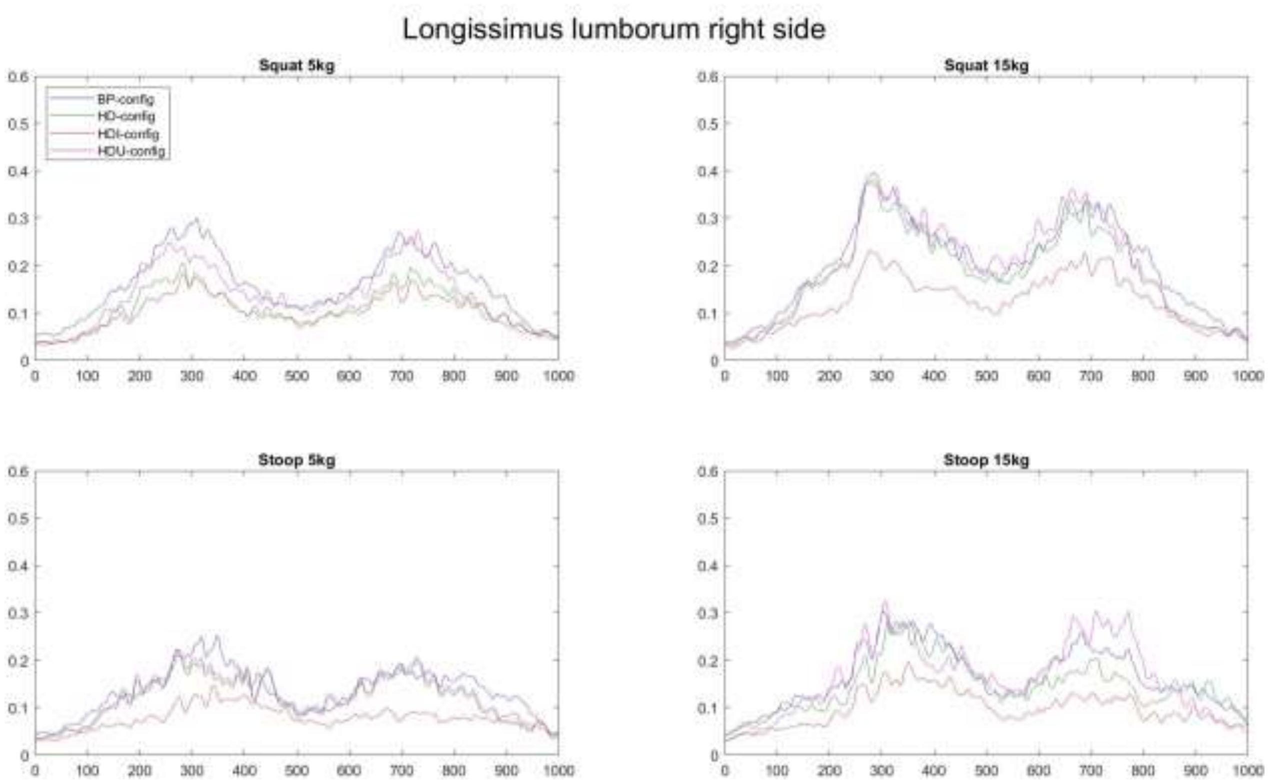

Fig. 2. Normalized EMG recordings of right longissimus lumborum muscle among four experimental conditions, and for BP-EMG, HD-EMG, HDI-EMG, and HDU-EMG configurations.

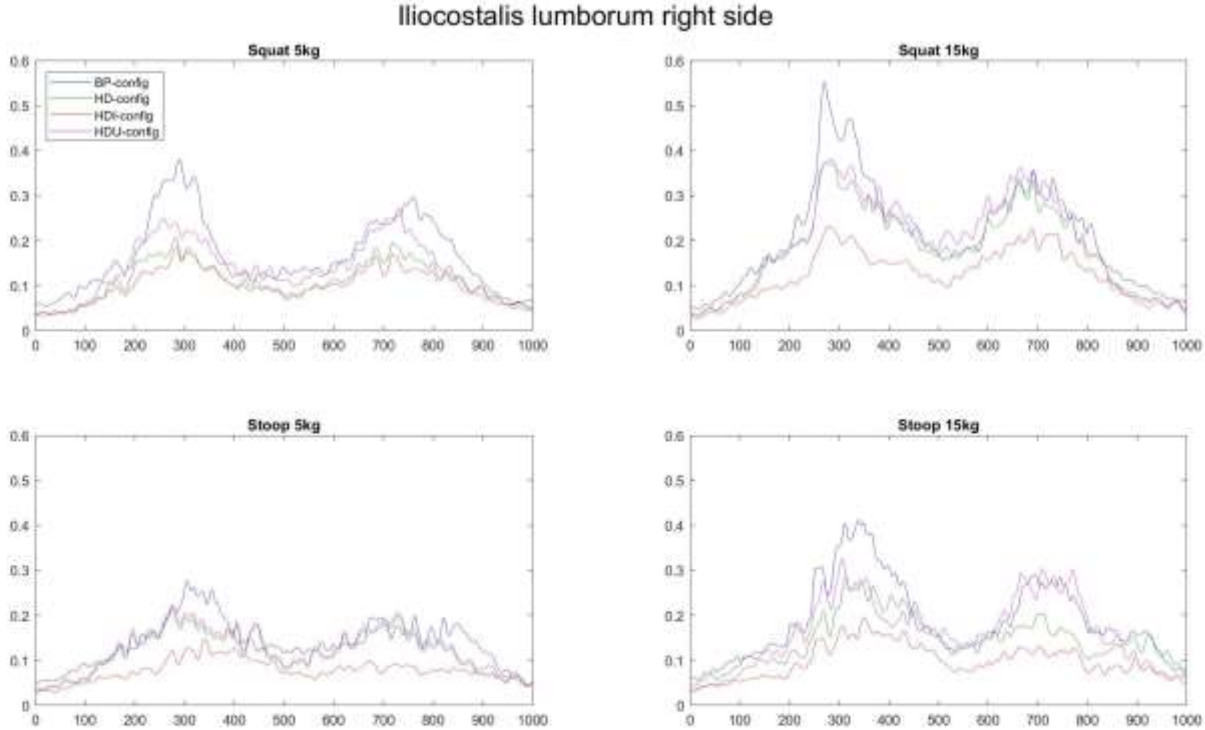

Fig. 3. Normalized EMG recordings of right iliocostalis lumborum muscle among four experimental conditions, and for BP-EMG, HD-EMG, HDI-EMG, and HDU-EMG configurations.

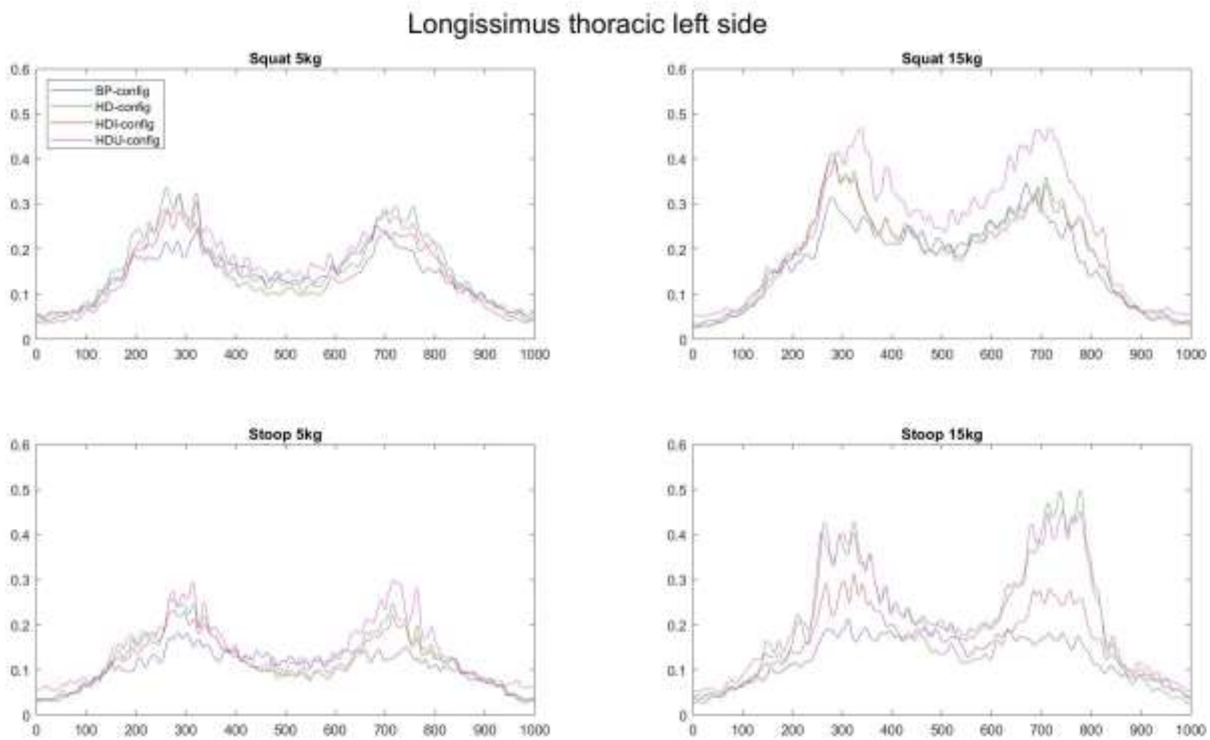

Fig. 4. Normalized EMG recordings of left longissimus thoracic muscle among four experimental conditions, and for BP-EMG, HD-EMG, HDI-EMG, and HDU-EMG configurations.

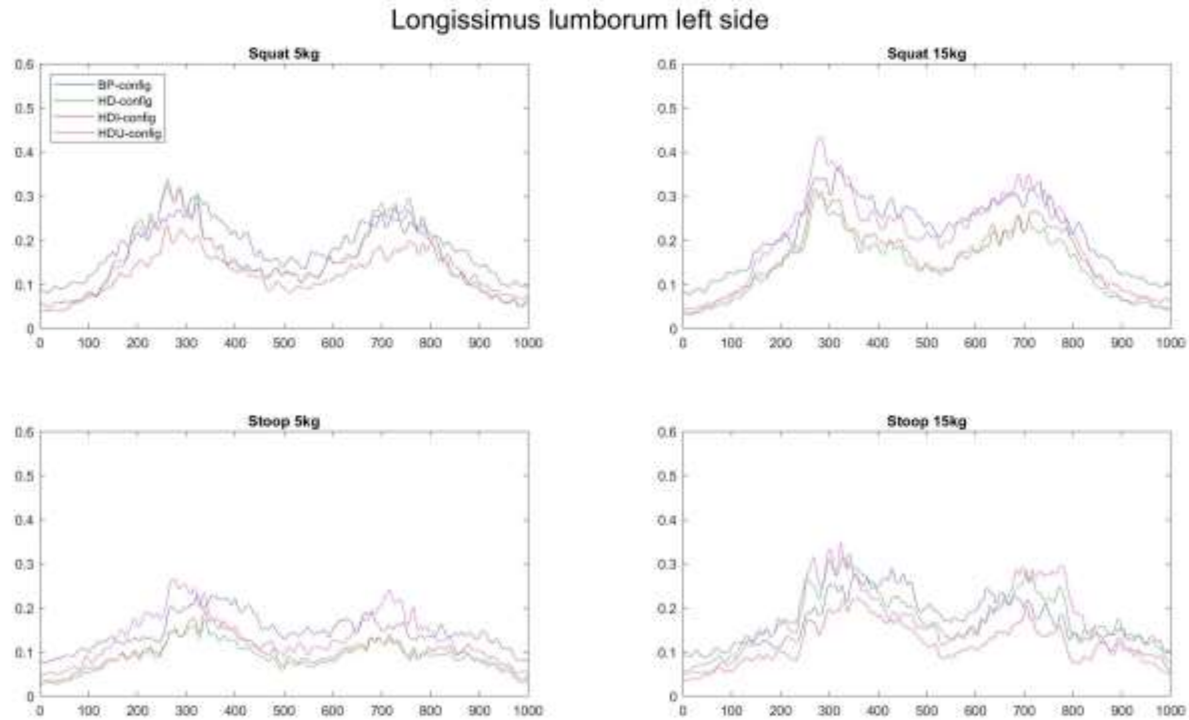

Fig. 5. Normalized EMG recordings of left longissimus lumborum muscle among four experimental conditions, and for BP-EMG, HD-EMG, HDI-EMG, and HDU-EMG configurations.

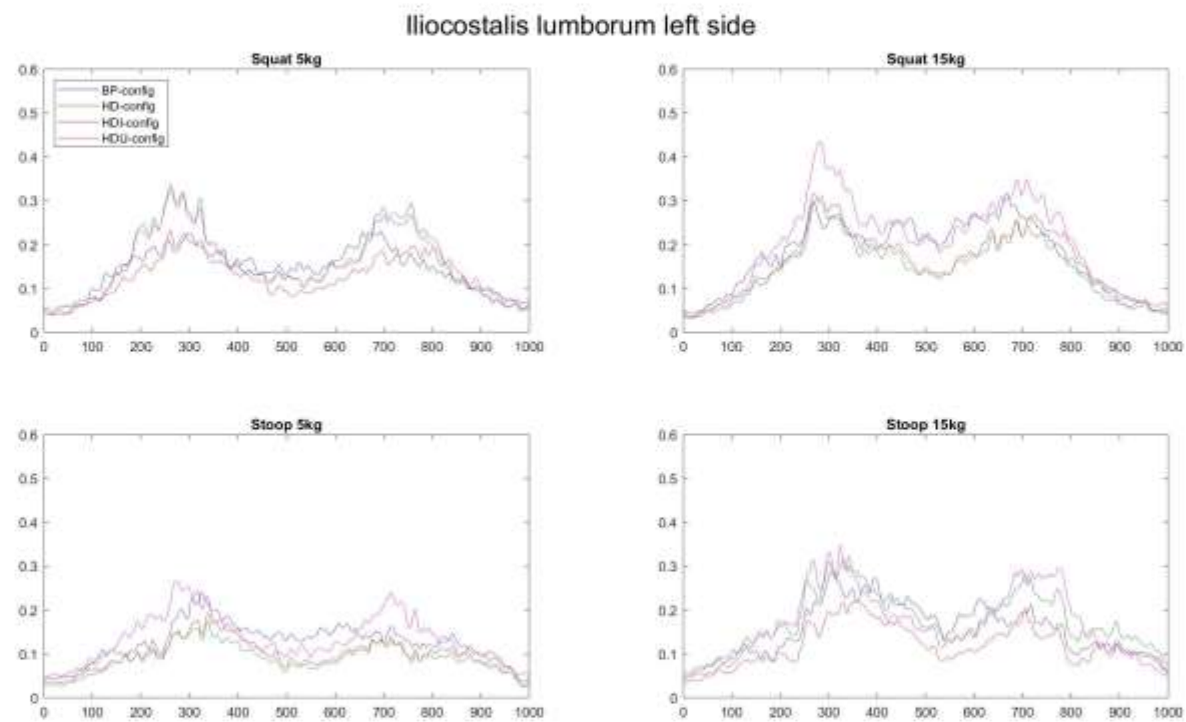

Fig. 6. Normalized EMG recordings of left iliocostalis lumborum muscle among four experimental conditions, and for BP-EMG, HD-EMG, HDI-EMG, and HDU-EMG configurations.

TABLE I
STRENGTH COEFFICIENTS OF BP-EMG AND HD-EMG CALIBRATED MODELS FOR DIFFERENT MUSCLE TENDON UNITS

Calibrated model using BP-EMG				**Calibrated model using HD-EMG**			
LTpT_T1_l	1	LTpT_T1_r	1	LTpT_T1_l	1	LTpT_T1_r	1
LTpT_T2_l	1	LTpT_T2_r	1	LTpT_T2_l	1	LTpT_T2_r	1
LTpT_T3_l	1	LTpT_T3_r	1	LTpT_T3_l	1	LTpT_T3_r	1
LTpT_T4_l	1	LTpT_T4_r	1	LTpT_T4_l	1	LTpT_T4_r	1
LTpT_T5_l	1	LTpT_T5_r	1	LTpT_T5_l	1	LTpT_T5_r	1
LTpT_T6_l	1	LTpT_T6_r	1	LTpT_T6_l	1	LTpT_T6_r	1
LTpT_T7_l	0.50000000007	LTpT_T7_r	0.50000000007	LTpT_T7_l	0.50000000208	LTpT_T7_r	0.50000000208
LTpT_T8_l	0.50000000007	LTpT_T8_r	0.50000000007	LTpT_T8_l	0.50000000208	LTpT_T8_r	0.50000000208
LTpT_T9_l	0.50000000007	LTpT_T9_r	0.50000000007	LTpT_T9_l	0.50000000208	LTpT_T9_r	0.50000000208
LTpT_T10_l	0.50000000007	LTpT_T10_r	0.50000000007	LTpT_T10_l	0.50000000208	LTpT_T10_r	0.50000000208
LTpT_T11_l	0.50000000007	LTpT_T11_r	0.50000000007	LTpT_T11_l	0.50000000208	LTpT_T11_r	0.50000000208
LTpT_T12_l	0.50000000007	LTpT_T12_r	0.50000000007	LTpT_T12_l	0.50000000208	LTpT_T12_r	0.50000000208
LTpT_R4_l	1	LTpT_R4_r	1	LTpT_R4_l	1	LTpT_R4_r	1
LTpT_R5_l	1	LTpT_R5_r	1	LTpT_R5_l	1	LTpT_R5_r	1
LTpT_R6_l	1	LTpT_R6_r	1	LTpT_R6_l	1	LTpT_R6_r	1
LTpT_R7_l	0.50000000007	LTpT_R7_r	0.50000000007	LTpT_R7_l	0.50000000208	LTpT_R7_r	0.50000000208
LTpT_R8_l	0.50000000007	LTpT_R8_r	0.50000000007	LTpT_R8_l	0.50000000208	LTpT_R8_r	0.50000000208
LTpT_R9_l	0.50000000007	LTpT_R9_r	0.50000000007	LTpT_R9_l	0.50000000208	LTpT_R9_r	0.50000000208
LTpT_R10_l	0.50000000007	LTpT_R10_r	0.50000000007	LTpT_R10_l	0.50000000208	LTpT_R10_r	0.50000000208
LTpT_R11_l	0.50000000007	LTpT_R11_r	0.50000000007	LTpT_R11_l	0.50000000208	LTpT_R11_r	0.50000000208
LTpT_R12_l	0.50000000007	LTpT_R12_r	0.50000000007	LTpT_R12_l	0.50000000208	LTpT_R12_r	0.50000000208
LTpL_L5_l	0.50000008451	LTpL_L5_r	0.50000008451	LTpL_L5_l	0.50000008451	LTpL_L5_r	0.50000008451
LTpL_L4_l	0.50000008451	LTpL_L4_r	0.50000008451	LTpL_L4_l	0.50000008451	LTpL_L4_r	0.50000008451
LTpL_L3_l	0.50000008451	LTpL_L3_r	0.50000008451	LTpL_L3_l	0.50000008451	LTpL_L3_r	0.50000008451
LTpL_L2_l	0.50000008451	LTpL_L2_r	0.50000008451	LTpL_L2_l	0.50000008451	LTpL_L2_r	0.50000008451
LTpL_L1_l	0.50000008451	LTpL_L1_r	0.50000008451	LTpL_L1_l	0.50000008451	LTpL_L1_r	0.50000008451
IL_L1_l	0.50000000051	IL_L1_r	0.50000000051	IL_L1_l	0.50000000114	IL_L1_r	0.50000000114
IL_L2_l	0.50000000051	IL_L2_r	0.50000000051	IL_L2_l	0.50000000114	IL_L2_r	0.50000000114
IL_L3_l	0.50000000051	IL_L3_r	0.50000000051	IL_L3_l	0.50000000114	IL_L3_r	0.50000000114
IL_L4_l	0.50000000051	IL_L4_r	0.50000000051	IL_L4_l	0.50000000114	IL_L4_r	0.50000000114
IL_R5_l	0.72449545298	IL_R5_r	0.72449545298	IL_R5_l	0.73308100372	IL_R5_r	0.73308100372
IL_R6_l	0.72449545298	IL_R6_r	0.72449545298	IL_R6_l	0.73308100372	IL_R6_r	0.73308100372
IL_R7_l	0.72449545298	IL_R7_r	0.72449545298	IL_R7_l	0.73308100372	IL_R7_r	0.73308100372
IL_R8_l	0.72449545298	IL_R8_r	0.72449545298	IL_R8_l	0.73308100372	IL_R8_r	0.73308100372
IL_R9_l	0.72449545298	IL_R9_r	0.72449545298	IL_R9_l	0.73308100372	IL_R9_r	0.73308100372
IL_R10_l	0.72449545298	IL_R10_r	0.72449545298	IL_R10_l	0.73308100372	IL_R10_r	0.73308100372
IL_R11_l	0.72449545298	IL_R11_r	0.72449545298	IL_R11_l	0.73308100372	IL_R11_r	0.73308100372
IL_R12_l	0.72449545298	IL_R12_r	0.72449545298	IL_R12_l	0.73308100372	IL_R12_r	0.73308100372